nature materials

Article

https://doi.org/10.1038/s41563-025-02207-9

Intermolecular-force-driven anisotropy breaks the thermoelectric trade-off in n-type conjugated polymers

Received: 3 June 2024

Accepted: 12 March 2025

Published online: 28 April 2025

Check for updates

Diego Rosas Villalva[1] ✉, Dennis Derewjanko[2], Yongcao Zhang[1], Ye Liu[1], Andrew Bates[3], Anirudh Sharma[1], Jianhua Han[1], Martí Gibert-Roca[1], Osnat Zapata Arteaga[1], Soyeong Jang[1], Stefania Moro[4], Giovanni Costantini[4], Xiaodan Gu[3], Martijn Kemerink[2] ✉ & Derya Baran[1] ✉

Controlling the molecular orientation of conjugated polymers is a vital yet complex process to modulate their optoelectronic properties along with boosting device performance. Here we propose a molecular-force-driven anisotropy strategy to modulate the molecular orientation of conjugated polymers. This strategy relies on the intermolecular interactions, gauged by the Hansen solubility parameters framework, to provide solvent selection criteria for conjugated polymers that render films with a preferential orientation. We showcase molecular-force-driven anisotropy to overcome the inverse coupling between the electrical conductivity and Seebeck coefficient in solution-processed organic thermoelectrics, a major challenge in the field. Our kinetic Monte Carlo simulations suggest that edge-on orientations break the trade-off by increasing the in-plane delocalization length. The molecular-force-driven anisotropy approach yields a power factor of 115 μW m^{-1} K^{-2} and a figure of merit of 0.17 at room temperature for the doped n-type 2DPP-2CNTVT:N-DMBI system. This power factor is 20 times larger than that of conventional doping approaches.

Conjugated polymers (CPs) exhibit a semiparacrystalline structure, with crystalline domains and defects embedded in an amorphous viscous matrix[1]. Their molecular orientation affects the performance of organic electronic devices. Vertical devices such as organic photovoltaics benefit from face-on orientations, whereas lateral devices such as thermoelectrics (TE) benefit from an edge-on orientation. Modulating the molecular orientation requires treatments, relying on trial and error before achieving reproducible results. Providing simple reproducible guidelines to texturize CP films is crucial.

In organic thermoelectrics (OTE), charge carriers migrate from the hot to the cold end, generating electric power (Fig. 1a) for waste heat recovery or power generation[2]. Performance of OTE is quantified by the figure of merit $ZT = \sigma S^2 T k^{-1}$, where σ is the electrical conductivity (S m^{-1}), S is the Seebeck coefficient (V K^{-1}), T is the absolute temperature (K) and k is the thermal conductivity (W m^{-1} K^{-1}). When k is unavailable, the power factor $PF = \sigma S^2$ serves as a performance proxy. OTEs use heavily doped organic semiconductors combining a π-CP or small molecule (host), with a chemical species (dopant). Their energy levels align to produce a charge transfer event (Fig. 1b), increasing the charge carrier density (n) and σ (ref. 3). The complementary architecture of OTE devices (Fig. 1c) requires both p- and n-type semiconductors to fabricate a full generator[4]. Moreover, p-type CPs

[1]Materials Science and Engineering Program (MSE), Physical Sciences and Engineering Division (PSE), King Abdullah University of Science and Technology (KAUST), Thuwal, Saudi Arabia. [2]Institute for Molecular Systems Engineering and Advanced Materials, Heidelberg University, Heidelberg, Germany. [3]School of Polymer Science and Engineering, The University of Southern Mississippi, Hattiesburg, MS, USA. [4]School of Chemistry, University of Birmingham, Birmingham, UK. ✉e-mail: diego.rosasvillalva@kaust.edu.sa; martijn.kemerink@uni-heidelberg.de; derya.baran@kaust.edu.sa

https://doi.org/10.1038/s41563-025-02207-9

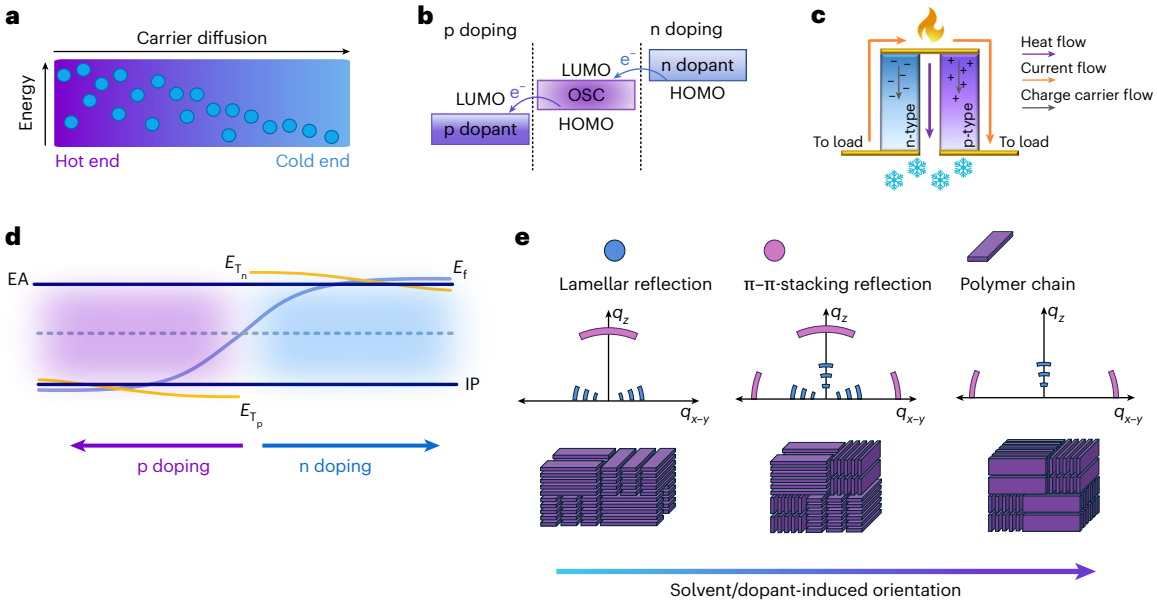

Fig. 1 | Fundamentals of organic TE and MFDA. a, Excitation of charge carriers at the hot end of a TE material, and their migration to the cold end, responsible for the Seebeck effect. **b**, Energetic alignment between the host and dopant, necessary for molecular doping. HOMO, highest occupied molecular orbital; LUMO; lowest unoccupied molecular orbital; OSC, organic semiconductor. **c**, Architecture of a single TE leg, depicting the flow of charges with respect to the temperature gradient. **d**, Schematic depicting the energetic origin of the TE trade-off. As doping increases and E_F shifts towards electron affinity (EA) or ionization potential (IP), the difference between E_F (Fermi level) and E_T (transport energy) narrows, thereby decreasing S. **e**, Schematic demonstrating the principle of MFDA in which the solvent and dopant control the orientation of polymer chain aggregates and the corresponding expected X-ray diffraction patterns.

showed robust performances from early stages, but n-type OTEs are more challenging[5–8]. Their poor host–dopant miscibility resulted in a low doping efficiency, hindering charge transport[9]. Novel chemical designs maximize σ by improving free charge carrier generation on doping[10–15]. Although successful, this approach encounters limitations due to the inverse relationship between σ and S. σ is defined by the charge carrier mobility (μ), charge density (n) and elementary charge (q) through the relationship $\sigma = \mu nq$ (ref. 16). Figure 1d illustrates the energetic origin of the TE trade-off. $S = E_F - E_T(qT)^{-1}$, where E_F is the Fermi level and E_T is the transport energy, which is the average energy of the moving charge carriers[17]; n and σ increase proportionally with dopant concentration. Simultaneously, E_F shifts towards electron affinity in n doping or towards ionization potential in p doping. As the difference between E_F and E_T decreases, S decreases[18]. Thus, σ and S hold an inverse relationship following the empirical power law $S \propto \sigma^{-1/4}$ (refs. 19,20). Overcoming this inverse relationship, known as the TE trade-off, is key to optimize the OTE performance.

Mechanical treatments generate aligned polythiophene films, increasing the delocalization length (α) and μ in the direction of rubbing or drawing[21–24]. This improves σ and S simultaneously, due to an anisotropic delocalization length[25–27]. Here we introduce the molecular-force-driven anisotropy (MFDA) strategy, which triggers a self-assembly process, yielding films with a preferential orientation. We establish the solvent selection criteria based on the solvent's boiling point (BP) and its Hansen solubility parameters (HSPs) to predict the molecular orientation of spin-coated CP films. MFDA leverages the natural tendency of solution-processed CPs to adopt edge-on or face-on orientations, enhancing in-plane σ without reducing S in OTEs, as confirmed by kinetic Monte Carlo (KMC) simulations. This approach allows the selective fabrication of high edge-on/face-on ratio (EFR) films, breaking the σ–S trade-off without additional processing.

MFDA also considers dopant effects on the film microstructure, demonstrating that dopants can reduce structural disorder. Using poly(2,5-bis(2-dodecylhexadecyl)-3,6-di(thiophen-2-yl) pyrrolo[3,4-c] pyrrole-1,4(2H,5H)-dione-*alt*-(E)-1,2-bis(3-cyanothiophen-2-yl)ethene) (2DPP-2CNTVT) as a model n-type CP with dopants 4-(2,3-dihydro-1,3-dimethyl-1H-benzimidazol-2-yl)-*N*,*N*-dimethylbenzenamine (N-DMBI), tetrabutylammonium fluoride (TBAF) and hexahydro-1H,3a^{1}H,4H,7H-3a,6a,9a-triazaphenalene (TAM), we show that blending 2DPP-2CNTVT with N-DMBI in chlorobenzene (CB) increases the edge-on fraction and crystallinity, extending the anisotropic α and yielding a maximum PF of 115 μW m^{-1} K^{-2}—20 times higher than using *ortho*-dichlorobenzene (*o*-DCB), the standard OTE solvent. This strategy also applies to p-type homopolymers like poly(3-hexylthiophene-2,5-diyl) (P3HT) and can be extended to other organic electronic devices such as organic field-effect transistors (OFETs) and organic electrochemical transistors[28–30].

Anisotropic transport in CPs

In CPs, charge delocalization occurs along the conjugated backbone (Fig. 2a) but is disrupted by defects such as kinks, twisting, branching points or homocoupling[31,32]. Long-range transport depends on interchain hopping via co-facial π–π contacts, with limited movement along insulating aliphatic side chains. In edge-on domains, α propagates coplanar to the film surface, whereas in face-on domains, it extends orthogonally. We conducted two simulation series: first, assuming homogeneous lattices with uniform boundary conditions, disregarding intra- versus interdomain hopping. Charge transport was modelled via KMC simulations using a nearest-neighbour hopping model with Abraham–Miller rates and a Gaussian density of states. Although dynamic disorder could be included, it is computationally prohibitive at the relevant length scales and does not affect our conclusions, which hinge on localization anisotropy rather than its static or dynamic nature[33,34].

Figure 2b depicts the spatial occupational probability of the charge delocalization length associated with the following five simulated cases: (1) an isotropic delocalization length vector $\alpha_{iso} = (\alpha_x\, \alpha_y\, \alpha_z) = 0.5 \times (1\,1\,1)$ nm; edge-on (2) and face-on (3) cases by setting the respective localization length vectors to $\alpha_{eo} = 0.5 \times (2\,2\,1)$ nm and $\alpha_{fo} = 0.5 \times (1\,1\,2)$ nm, respectively, where the in-plane direction is

https://doi.org/10.1038/s41563-025-02207-9

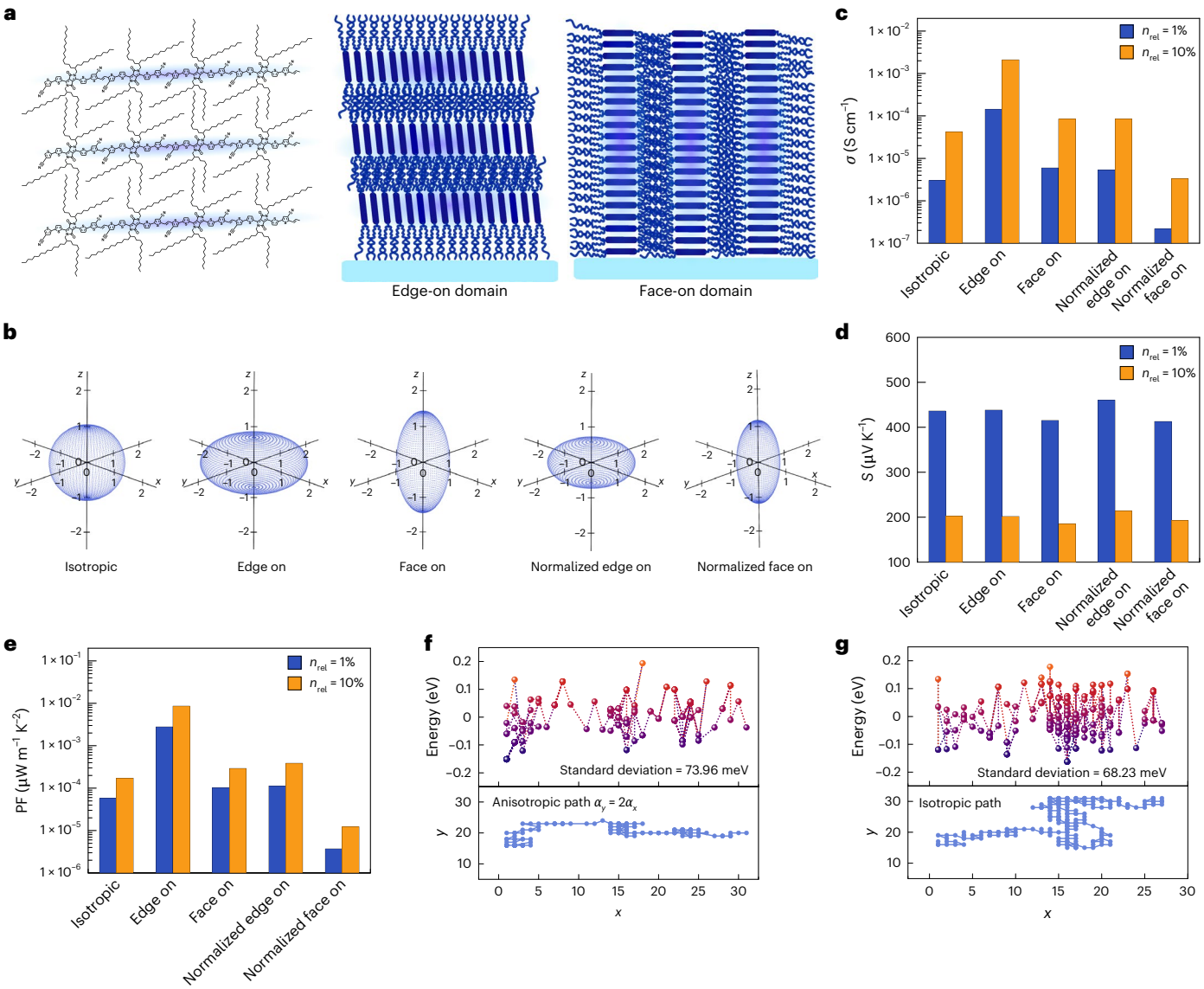

Fig. 2 | KMC modelling of isotropic and anisotropic systems. a, Schematic showing the intrachain charge delocalization along the π-conjugated backbone (left) and the interchain charge delocalization along the π–π stacking (middle and right) as a purple cloud. In the edge-on case, it extends parallel to the plane of the substrate, whereas in the face-on case, it extends perpendicularly. **b**, Surfaces representing the spatial distribution of the delocalization vectors for the simulated cases. **c**–**e**, Simulation results for σ (**c**), S (**d**) and PF (**e**). n_{rel} is the relative increase in charge carrier density as charge density per density of states; that is, for n_{rel} = 1%, 1 out of every 100 states is occupied by a charge. **f**,**g**, Projection of the charge hopping path in the energy space (top) and real space, with x and y being the lattice sites in each corresponding direction (bottom) for the anisotropic (**f**) and isotropic (**g**) cases.

set to be the x–y plane of the system; (4) and (5) localization length vectors were normalized by rescaling the anisotropic localization length vector to have the same length as the isotropic case. Morphologically, normalized cases reflect film reorganization into a preferential orientation, whereas the non-normalized cases exemplify a reorganization into a preferential orientation, plus an increase in the crystalline portion of the film, that is, larger crystalline domains, or a larger population of crystallites. Each case is simulated at two relative charge carrier densities (n_{rel}) (1% and 10%). The calculated in-plane TE properties (Fig. 2c–e) show that the edge-on cases enhance σ and PF compared with isotropic and face-on cases. Additionally, a slight increase in S suggests that this molecular orientation is beneficial to overcome the TE trade-off.

It is not evident that an inhomogeneous film consisting predominantly of edge-on domains can be described as an anisotropic but otherwise homogeneous system, as in the previous set of simulations, that is, with an in-plane enhancement in the localization length that is equal everywhere. Therefore, we carried out a second set of simulations, introducing a subprogram that generates polymer morphologies based on a three-phase model (Supplementary Fig. 1), allowing to account for aggregation-induced inhomogeneities and, accordingly, in charge transport (Supplementary Note 1)[35]. Supplementary Fig. 2a,b shows a cube and a slice of the generated film's morphology with a preferential edge-on orientation. We introduced two delocalization enhancement factors within the generated morphology. First, f_{ich} increases with facile intrachain transport, in the absence of twists, kinks and/or branching points. Second, f_{α} accounts for facile interchain transport along the π–π-stacking direction. Intra-aggregate transport is substantially enhanced over interaggregate transport as aggregate boundaries are characterized by a high degree of conformational defects and/or a low degree of π–π stacking. The calculated OTE properties (Table 1) confirm the results for homogeneous systems. As we increase either

https://doi.org/10.1038/s41563-025-02207-9

Table 1 | Calculated in-plane Seebeck coefficient and electrical conductivity for edge-on morphologies

	$f_{ich}=f_{\alpha}=1.0$	$f_{ich}=1.25, f_{\alpha}=1.0$	$f_{ich}=1.0, f_{\alpha}=1.5$	$f_{ich}=1.25, f_{\alpha}=1.5$
S (μV K^{-1})	697±4	704±5	715±3	734±3
σ (S cm^{-1})	14.7±0.1	19.0±0.1	22.7±0.1	29.3±0.3

The edge-on morphologies are generated using a three-phase model for different combinations of delocalization enhancement factors of f_{ich} and f_{α}. Other hopping parameters used are the same as those shown in Fig. 1.

of the enhancement factors—accounting for the inherent anisotropy of charge transport in CP systems—σ and S increase simultaneously, further evidence that an edge-on orientation decouples the trade-off between σ and S.

Three-dimensional (3D) KMC simulations further elucidate the TE trade-off decoupling. Figure 2f,g shows the charge hopping paths in energy space for anisotropic and isotropic films, respectively, with the anisotropic case exhibiting a linear path. For the two given hopping sites with the same energy difference, there is a larger probability of hopping in the direction of the larger delocalization length, as given by the tunnelling term in the Miller–Abraham rate. Thus, for the same total hopping probability, a charge can overcome a larger energy difference in the direction of larger delocalization. The more direct path translates into a higher velocity in the direction of larger delocalization, that is, higher electrical conductivity. Simultaneously, this produces jumps over larger energy differences, resulting in a higher transport energy, and an increased S.

Solvent-driven anisotropy

Preaggregates in solution modulate the molecular orientation of CP films (Fig. 3a)[28–30]. HSPs quantify and represent the molecular interactions of chemical species in 3D space[36]. HSPs consider the dispersive (δD), polar (δP) and hydrogen-bonding (δH) intermolecular forces of multiple instances of the same chemical species interacting together. Each force is assigned to an axis of Cartesian space, generating a 3D coordinate system in which solvents are located by their δD, δP and δH values. Solutes are represented by a solubility sphere (SS) with a centre of (δD, δP, δH) and radius R_0 for a given temperature and concentration. If the Hansen distance (R_a) between the centroids of the solute and the solvent is smaller than R_0, the solvent is within the SS and should solubilize the solute (Supplementary Fig. 3). Centroids that lie at the edge or in the periphery of the SS are partial solvents, that is, the solute solubilizes at low concentrations or high temperatures. At small R_a, the affinity of the solvent for the CP increases, leading to fully dissociated polymer chains that produce spin-coated films with the face-on orientation. Larger R_a renders solution preaggregates and, thus, edge-on orientation. We also consider the BP of the solvent since previous studies show its influence on the molecular orientation, microstructure and charge transport properties of the CP film[37].

We test this hypothesis using 2DPP-2CNTVT (Fig. 3b), owing to the recent demonstration of high OTE performance in DPP CPs[38–42]. We also studied the influence of three n-type dopants on molecular packing, namely, N-DMBI, TBAF and TAM. We determined the HSP and SS of 2DPP-2CNTVT (Fig. 3c) using a multiple-solvent approach (details in Supplementary Technical Note 2), with R_0 = 5.4 MPa$^{1/2}$ at room temperature and 10 mg ml^{-1}. Supplementary Fig. 4 compares the spheres at room temperature and 100 °C in 3D and 2D projections. We selected a set of solvents with varying R_a values ranging from the central region to the outer periphery of the SS (Supplementary Table 1) and used them to spin coat films of 2DPP-2CNTVT. Their molecular orientation was determined using grazing-incidence wide-angle X-ray scattering (GIWAXS). The 2D diffractograms (Supplementary Figs. 5 and 6) demonstrate a clear tendency of the good solvents ($R_a < R_0$) to create a face-on or bimodal packing, whereas the partial solvents ($R_a \geq R_0$) tend to generate a dominant edge-on orientation, further evidenced in the linecuts (Supplementary Fig. 7a,b) and the azimuthal integration of the (010) reflection in Supplementary Fig. 7c, which shows the migration of the reflection from the meridian (90°) to the equator (0° and 180°).

R_a is not the only factor responsible for the orientation of these films. For instance, tetrahydrofuran (THF), at the edge of the SS, produces a face-on orientation, whereas *o*-DCB with the smallest R_a value within this set, yields a dominant edge-on orientation, possibly resulting from the solvents' higher BP (Fig. 3g). We calculated the EFR from all diffractograms, dividing the integrated area of the (100) out-of-plane reflection by that of the in-plane (100) reflection. Supplementary Fig. 8a,b shows a proportional but non-systematic increment in EFR versus either R_a or BP. We used the product of R_a and BP (Supplementary Fig. 8c) to produce a more systematic trend that follows an exponential curve. These data show that the product of R_a and BP is a good parameter to estimate the molecular orientation that a given solvent will convey to a CP film. In particular, solvents that lie within the SS tend to produce a face-on or bimodal packing (as their R_a increases), and partial solvents (lying at the edge or outside the SS) tend to promote a dominant edge-on orientation.

To test the general applicability of this selection criterion to other CPs, we tested it on the p-type CP P3HT (Fig. 3e and Supplementary Figs. 9–12) and another n-type CP, poly([*N*,*N*′-bis(2-octyldodecyl) naphthalene-1,4,5,8-bis(dicarboximide)-2,6-diyl]-*alt*-5,5′-(2,2′-bithiophene)) (N2200; Fig. 3f and Supplementary Figs. 13 and 14). P3HT follows a similar trend to 2DPP-2CNTVT with an incremental EFR as either R_a or BP increases. Conversely, N2200 kept a pure face-on orientation across different solvents. P3HT and 2DPP-2CNTVT have conjugated backbones with relatively small dihedral angles that allow lamellar aggregation that is, about 0° (refs. 14,43,44). N2200 has a large dihedral angle between the naphtalenediimide (NDI) and bithiophene subunits (about 60°), causing a twisted backbone[45,46]. We propose that this twist induces different solution aggregation modes that prevent the formation of lamellae, hindering the development of an edge-on orientation.

Dopant-driven anisotropy

Typically, the dopant is regarded as a source of structural disorder, but some studies show an improvement in the molecular packing on the addition of dopants[47–49]. We propose that some dopants act as additives, where the dopant—added in solution—would interact with the CP and displace the solvent molecules. Since the dopant is also a solute, the interaction reduces the solubility of the polymer–dopant complex in the solvent, triggering CP nucleation. This results in an increase in the crystalline fraction and the edge-on portion of the dried CP film, as observed for partial solvents.

To test this, we obtained the HSPs for N-DMBI, TAM and TBAF and plotted them along with the SS of 2DPP-2CNTVT. N-DMBI has the highest affinity for 2DPP-2CNTVT, that is, the smallest R_a, and has the highest potential of triggering the desired effect. The other two dopants are located outside the SS. Doping probably introduces charged species into the system, but determining their HSPs would be exceedingly complex, time-intensive and impractical. The doping efficiency of N-DMBI is estimated to be between 0.5% and 1% (refs. 9,50). Consequently, the remaining 99.5–99% of neutral polymers and dopants dominate the assembly of the thin-film morphology, rather than the minimal fraction of ionized species. Therefore, we conclude that the influence of the HSPs of ionic species on the texturization of doped CP thin films can be safely neglected when using a relatively inefficient dopant; more efficient dopants might cause the model to fail.

We blended 2DPP-2CNTVT with 20 mol% N-DMBI in the previous solvents and spin-coated films from these solutions; the GIWAXS data are shown in Supplementary Figs. 15–17. The change in the EFR of the doped films with respect to the non-doped films is expressed as ΔEFR/EFR (Fig. 3g). At small solvent R_a, the dopant is unable to displace the solvent molecules in solution. As the solvent R_a value increases, its

https://doi.org/10.1038/s41563-025-02207-9

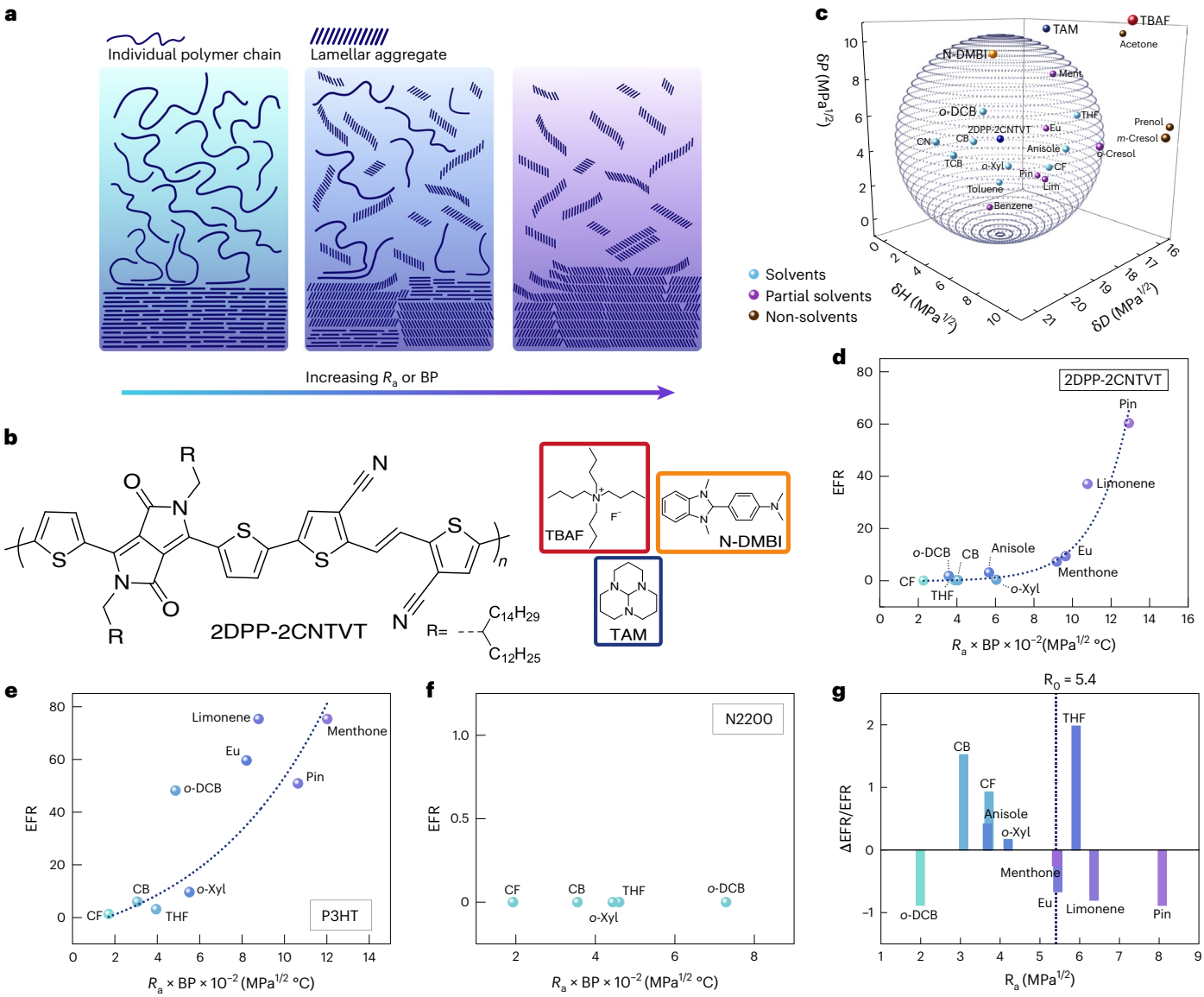

Fig. 3 | Phenomenological model of MFDA. a, Schematic of the MFDA process in which the solution aggregates modulate the molecular orientation of the film. Fully dissociated CP chains in the left schematic are more likely to land flat on the substrate on deposition, resulting in a face-on film; this is the case for good solvents. As the CP solubility decreases, chains aggregate co-facially in solution, forming lamellae that can land as a single entity. Solvents that cannot fully dissociate the CP aggregates will generate a bimodal texture (middle schematic). Partial solvents can solubilize the CP but have a large population of lamellar aggregates, resulting in a preferential edge-on orientation (right schematic). **b**, Chemical structures of 2DPP-2CNTVT and the molecular dopants. **c**, SS of 2DPP-2CNTVT at room temperature. **d**–**f**, EFR versus the product of R_a and BP for 2DPP-2CNTVT (**d**), P3HT (**e**) and N2200 (**f**). **g**, Normalized change in the EFR of 2DPP-2CNTVT on the addition of 20 mol% N-DMBI in different solvents. A positive value indicates an increase in the EFR, observed mostly within an R_a range of 3–4 MPa$^{1/2}$.

affinity for the CP decreases and the dopant can displace the solvent molecules. The R_a value of N-DMBI to the solvents and 2DPP-2CNTVT (Extended Data Fig. 1) suggests that N-DMBI is equally likely to interact with either *o*-DCB or 2DPP-2CNTVT, but it is less likely to interact with CB (Extended Data Fig. 2). For solvents with R_a larger than R_0, the population of aggregates hinders the ability of N-DMBI to intercalate with the CP, resulting in either phase segregation (such as in the case of THF) or a decrease in the EFR (as in terpenoid solvents).

Since CB showed the highest increment in the EFR, we decided to blend the rest of the dopants with 2DPP-2CNTVT using this solvent to study the role of different dopants on the microstructure. Atomic force microscopy (AFM) scans (Fig. 4a) showed a similar topography between the pristine film and those at 20 mol% dopant. At 40 mol% (Supplementary Fig. 18), TBAF doping formed large dopant clusters, agreeing with its large R_a value versus 2DPP-2CNTVT. At this concentration, TAM and N-DMBI still show minimal differences. AFM coupled with infrared spectroscopy (AFM-IR) maps the film composition at 20 mol% dopant loading (Fig. 4b and Supplementary Fig. 19). 2DPP-2CNTVT (green channel) forms fibrillar domains with an average diameter of 142 nm. TBAF, N-DMBI and TAM (red channel) reduce the domain size to 95 nm, 111 nm and 140 nm, respectively. TBAF drastically increases the structural disorder. TAM, on the other hand, barely changes the domain size, as previously reported for other CPs[48,51].

We performed GIWAXS on the doped films at different dopant concentrations (Fig. 4c, Supplementary Figs. 20 and 21 and Supplementary Tables 3 and 4) to understand the dopant intercalation with 2DPP-2CNTVT and its effect on molecular packing. N-DMBI and TAM maintain their native lamellar *d* spacing, whereas it increases for TBAF at small concentrations and decreases at higher values, suggesting phase segregation in agreement with the AFM scans (Fig. 4d). The π–π

https://doi.org/10.1038/s41563-025-02207-9

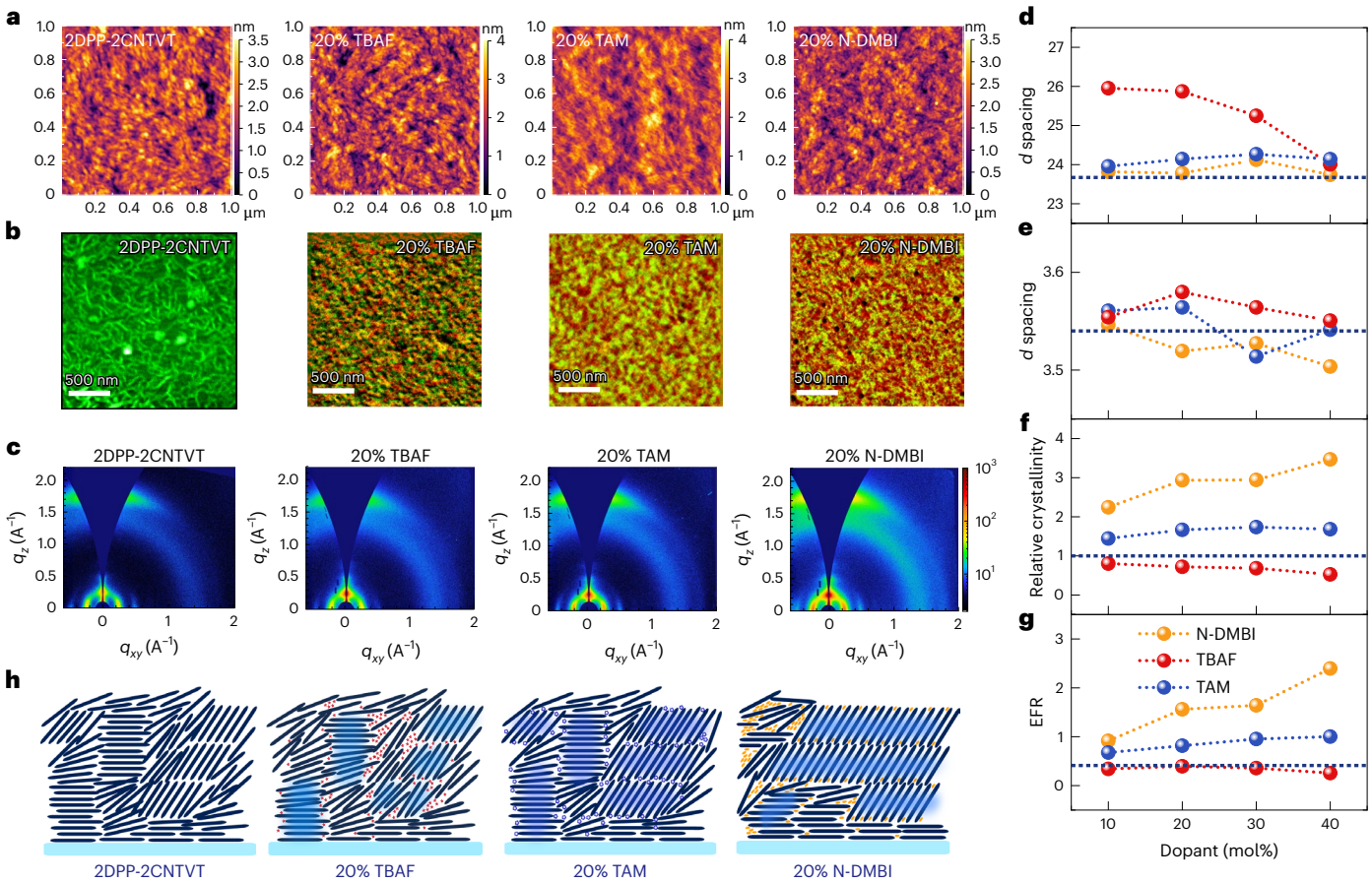

Fig. 4 | Influence of different molecular dopants on the microstructure of 2DPP-2CNTVT. a,**b**, AFM topography image (1 μm × 1 μm; **a**) and AFM-IR scans (2 μm × 2 μm; **b**) of pristine and doped 2DPP-2CNTVT films spin-coated from CB. The green channel is assigned to 2DPP-2CNTVT at 1,670 cm^{-1}. The red channel is assigned to the dopant, that is, N-DMBI at 1,552 cm^{-1}, TAM at 1,555 cm^{-1} and TBAF at 1,481 cm^{-1}. **c**, GIWAXS diffractograms obtained under the same conditions as AFM. **d**–**g**, Lamellar *d* spacing (**d**), π–π *d* spacing (**e**), relative crystallinity (**f**) and EFR (**g**) as obtained from the GIWAXS linecuts. The horizontal dark-blue dashed line shows the value for the non-doped 2DPP-2CNTVT. **h**, Schematic depicting the microscale morphology of 2DPP-2CNTVT films after doping. The pristine film shows a bimodal packing with both edge-on and face-on orientations. TBAF (red stars) reduces the crystallinity of the film and generates aggregates. TAM (blue pentagons) intercalates with 2DPP-2CNTVT, leaving the native structure unmodified. N-DMBI (yellow ellipses) increases the crystallinity and edge-on portion of the film.

d spacing is slightly decreased by N-DMBI, whereas slightly increased by TBAF. We integrated the area of both in-plane and out-of-plane (100) reflections to estimate the crystalline fraction and EFR of the doped films and compared them with those of pristine 2DPP-2CNTVT (Fig. 4f). N-DMBI increases both crystalline fraction (Fig. 4g) of 2DPP-2CNTVT and EFR to the highest extent. Figure 3h shows a schematic of the resulting film morphologies from the three doping cases. 2DPP-2CNTVT starts with a bimodal texture; the addition of TBAF—with the largest R_a—increases the structural disorder and decreases the EFR, limiting the delocalization length and charge transport properties. TAM, with an intermediate R_a, intercalates with the CP, moderately improving the crystallinity and the EFR. Finally, N-DMBI produces the largest increase in the EFR, and crystallinity attributed to having the smallest R_a amongst the three dopants and still being contained within the SS of 2DPP-2CNTVT.

Electronic properties of oriented CP films

We tested the efficacy of MFDA on improving the performance of OFETs fabricated from P3HT (Fig. 5a) and 2DPP-2CNTVT (Fig. 5b). OFETs benefit from an edge-on orientation. As we fabricated transistors from solvents that increase the EFR, we observed improvements in the current–voltage (*I*–*V*) characteristics for both OFET series. Face-on-oriented solvents produce small ON–OFF current ratios, lower mobility and high subthreshold swing. As we replace the solvent by those producing a higher EFR, the ON–OFF current ratio and mobility increase, whereas the subthreshold swing decreases for both P3HT and 2DPP-2CNTVT OFETs. Next, we tested the in-plane κ value of 2DPP-2CNTVT films cast from chloroform (CF), CB, eucalyptol (Eu) and pinene (Pin), yielding values of 0.21 W m^{-1} K^{-1}, 0.16 W m^{-1} K^{-1}, 0.15 W m^{-1} K^{-1} and 0.14 W m^{-1} K^{-1}, respectively (Fig. 5c), suggesting an inverse relationship between the EFR and in-plane κ.

We evaluated the OTE properties of 2DPP-2CNTVT doped in CB (Supplementary Figs. 22 and 23). TBAF-doped films have low σ (Supplementary Fig. 23a) and high *S* (Supplementary Fig. 23b), whereas TAM-doped films show the opposite, in agreement with the AFM-IR morphological characterization. Despite the different values, both series of films display OTE properties that align with the same power law, that is, $S \propto \sigma^{-1/4}$ (Fig. 5d), thereby limiting their PF. By contrast, N-DMBI achieves higher σ values than TBAF but an *S* value that is as high as that of TBAF-doped films, resulting in a deviation from the power law and yielding higher OTE properties. We ascribe this to the higher EFR and crystalline fraction of N-DMBI-doped films. Photoelectron spectroscopy, ultraviolet–visible and thermal activation energy measurements (Supplementary Figs. 24–26) discard the possibility that differences in performance stem from different doping efficiencies and/or *n*.

https://doi.org/10.1038/s41563-025-02207-9

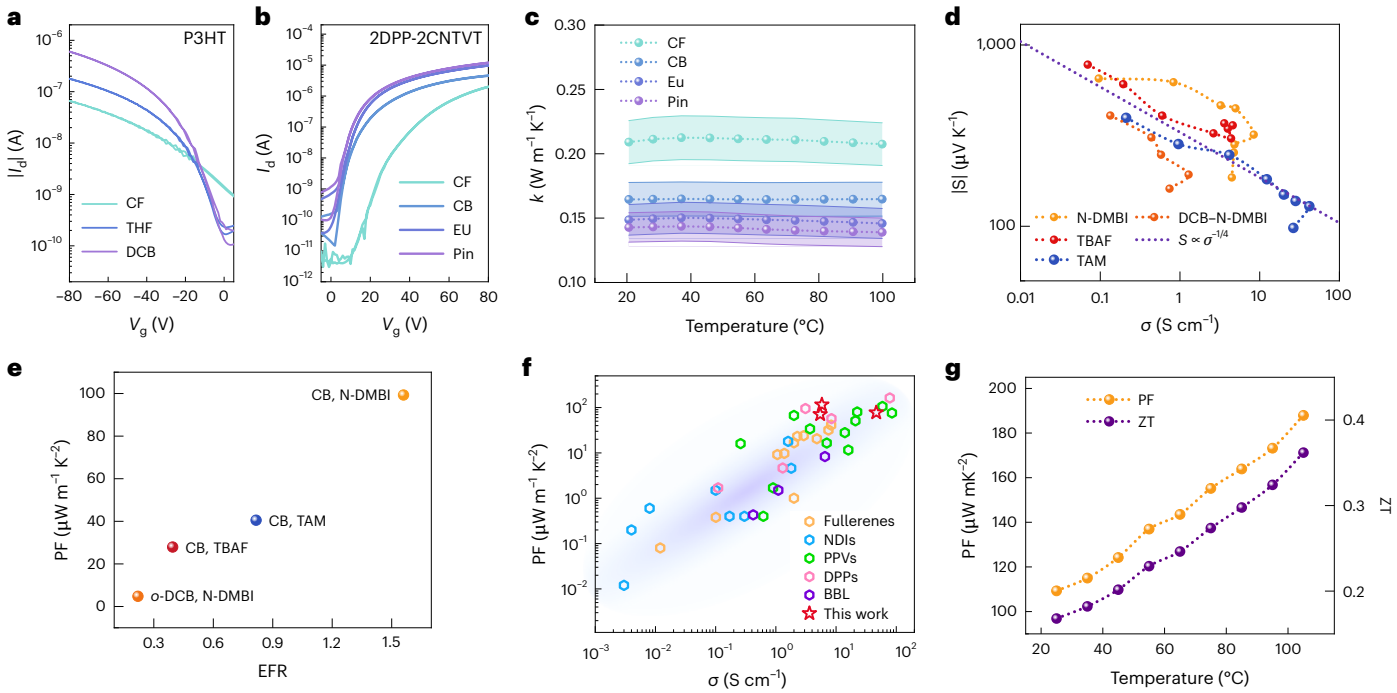

Fig. 5 | Charge transport and TE properties of texturized 2DPP-2CNTVT. **a**,**b**, Transistor I–V characteristics for P3HT (**a**) and 2DPP-2CNTVT (**b**) films cast from different solvents. The linear mobility and ON–OFF ratio increase along with the EFR. **c**, T-dependent κ of 2DPP-2CNTVT films cast from different solvents. Although the change is rather obvious from CF to CB, the differences between CB, Eu and Pin are within the instrument-induced error (as shown by the error bands); caution is advised in the interpretation of these results. **d**, TE properties of doped films. **e**, PF versus EFR at 20 mol% dopant loading. **f**, PF versus σ of previously reported n-type OTEs; the blue-shaded area is a visual guidance denoting the trend of the reported OTE PF values, including *para*-phenylene vinylene (PPV) based-polymers and poly(benzimidazobenzophenanthroline) (BBL). A list and the corresponding references are provided in Supplementary Table 5. **g**, Temperature-dependent PF and ZT of 2DPP-2CNTVT + 20 mol% N-DMBI.

Finally, we conducted a series of experiments following procedures reported in the literature to compare the OTE output with those versus the MFDA approach. First, we sequentially doped 2DPP-2CNTVT films with N-DMBI and TAM (their OTE properties are summarized in Supplementary Fig. 27). Sequential N-DMBI doping yields lower performance compared with the MFDA approach. Structural characterization (Supplementary Fig. 28) shows no enhancement, neither in the crystalline fraction nor in the EFR of sequentially doped samples. This supports the conclusion that structural enhancement originates from the interplay between the intermolecular interactions of host, dopant and solvent.

Second, we used *o*-DCB, one of the most common solvents used in OTEs, to blend 2DPP-2CNTVT and N-DMBI. The resulting PF is around 20 times lower compared with CB due to the lower EFR (Fig. 5e). In particular, the PF increases proportionally for films with higher EFR. Films doped with N-DMBI in CB produce a maximum PF of 115 μW m^{-1} K^{-2}. These values are amongst the highest reported PFs for n-type OTEs (Fig. 5f), demonstrating the importance of the careful selection of solvent–host–dopant combinations.

We measured the temperature-dependent OTE properties of the 2DPP-2CNTVT film with 20 mol% N-DMBI loading (Supplementary Fig. 29). The film shows a classical semiconducting behaviour, that is, increasing σ and decreasing S as the temperature increases. κ remains constant across the probed range, at about 0.2 W m^{-1} K^{-1}. This results in a ZT value of 0.17 at room temperature and 0.36 at 100 °C (Fig. 5g). These values are amongst the highest reported for n-type OTEs, showing the potential of MFDA to maximize performance.

Outlook

In summary, we introduced the MFDA approach that bridges the gap between processing conditions, material properties and device performance. MFDA relies on the intermolecular forces acting between solvents, dopants and CPs, to increase the tendency of CPs to pack following a preferential orientation when spin coated. The HSP approach provides a semiquantitative framework to select a combinations of CPs, dopants and solvents that trigger a self-assembly process, yielding a morphology beneficial for charge transport in an electronic device. We recognize that our model is limited to materials with at least a certain degree of crystallinity, and that we cannot account for charge transport through amorphous regions. Although novel chemical designs enhanced the performance of OTEs, MFDA is an additional tool for the further enhancement of device performance. Our findings show that OTEs benefit from MFDA when it is tailored to generate an edge-on orientation, owing to its ability to break the TE trade-off. The generality of the HSP model suggests that these guidelines extend to other CPs, as exemplified by the texturization of P3HT. Thus, this work provides a valuable tool for advancing and optimizing the microscale morphology of organic electronic materials for devices that would benefit from a preferential molecular orientation to control and maximize performance.

Online content

Any methods, additional references, Nature Portfolio reporting summaries, source data, extended data, supplementary information, acknowledgements, peer review information; details of author contributions and competing interests; and statements of data and code availability are available at https://doi.org/10.1038/s41563-025-02207-9.

References

1. Marina, S. et al. Semi-paracrystallinity in semi-conducting polymers. *Mater. Horiz.* **9**, 1196–1206 (2022).
2. Cowen, L. M., Atoyo, J., Carnie, M. J., Baran, D. & Schroeder, B. C. Review—organic materials for thermoelectric energy generation. *ECS J. Solid State Sci. Technol.* **6**, N3080–N3088 (2017).

3. Tietze, M. L. et al. Elementary steps in electrical doping of organic semiconductors. *Nat. Commun.* **9**, 1182 (2018).
4. Bubnova, O. & Crispin, X. Towards polymer-based organic thermoelectric generators. *Energy Environ. Sci.* **5**, 9345–9362 (2012).
5. Bubnova, O. et al. Optimization of the thermoelectric figure of merit in the conducting polymer poly(3 ,4-ethylenedioxythiophene). *Nat. Mater.* **10**, 429–433 (2011).
6. Villalva, D. R., Haque, M. A., Nugraha, M. I. & Baran, D. Enhanced thermoelectric performance and lifetime in acid-doped PEDOT:PSS films via work function modification. *ACS Appl. Energy Mater.* **3**, 9126–9132 (2020).
7. Patel, S. N. et al. Morphology controls the thermoelectric power factor of a doped semiconducting polymer. *Sci. Adv.* **3**, e1700434 (2017).
8. Liu, Z. et al. Enhancement of the thermoelectric performance of DPP based polymers by introducing one 3,4-ethylenedioxythiophene electron-rich building block. *J. Mater. Chem. C* **8**, 10859–10867 (2020).
9. Schlitz, R. A. et al. Solubility-limited extrinsic n-type doping of a high electron mobility polymer for thermoelectric applications. *Adv. Mater.* **26**, 2825–2830 (2014).
10. Liu, J. et al. Amphipathic side chain of a conjugated polymer optimizes dopant location toward efficient n-type organic thermoelectrics. *Adv. Mater.* **33**, e2006694 (2021).
11. Rosas Villalva, D. et al. Backbone-driven host-dopant miscibility modulates molecular doping in NDI conjugated polymers. *Mater. Horiz.* **9**, 500–508 (2022).
12. Liu, J. et al. N-type organic thermoelectrics: demonstration of ZT > 0.3. *Nat. Commun.* **11**, 5694 (2020).
13. Shi, K. et al. Toward high performance n-type thermoelectric materials by rational modification of BDPPV backbones. *J. Am. Chem. Soc.* **137**, 6979–6982 (2015).
14. Yan, X. et al. Pyrazine-flanked diketopyrrolopyrrole (DPP): a new polymer building block for high-performance n-type organic thermoelectrics. *J. Am. Chem. Soc.* **141**, 20215–20221 (2019).
15. Gamez-Valenzuela, S. et al. High-performance n-type organic thermoelectrics with exceptional conductivity by polymer-dopant matching. *Angew. Chem. Int. Ed.* **63**, e202408537 (2024).
16. Brunetti, I., Dash, A., Scheunemann, D. & Kemerink, M. Is the field of organic thermoelectrics stuck? *J. Mater. Res.* **39**, 1197–1206 (2024).
17. Liang, Z. et al. n-type charge transport in heavily p-doped polymers. *Nat. Mater.* **20**, 518–524 (2021).
18. Xu, K. et al. On the origin of Seebeck coefficient inversion in highly doped conducting polymers. *Adv. Funct. Mater.* **32**, e2112276 (2022).
19. Untilova, V. et al. High thermoelectric power factor of poly(3-hexylthiophene) through in-plane alignment and doping with a molybdenum dithiolene complex. *Macromolecules* **53**, 6314–6321 (2020).
20. Upadhyaya, M., Boyle, C. J., Venkataraman, D. & Aksamija, Z. Effects of disorder on thermoelectric properties of semiconducting polymers. *Sci. Rep.* **9**, 5820 (2019).
21. Hynynen, J. et al. Enhanced thermoelectric power factor of tensile drawn poly(3-hexylthiophene). *ACS Macro Lett.* **8**, 70–76 (2019).
22. Qu, S. et al. Highly anisotropic P3HT films with enhanced thermoelectric performance via organic small molecule epitaxy. *NPG Asia Mater.* **8**, e292 (2016).
23. Vijayakumar, V. et al. Bringing conducting polymers to high order: toward conductivities beyond 10^5 S cm^{-1} and thermoelectric power factors of 2 mW m^{-1} K^{-2}. *Adv. Energy Mater.* **9**, e1900266 (2019).
24. Vijayakumar, V. et al. Influence of dopant size and doping method on the structure and thermoelectric properties of PBTTT films doped with F6TCNNQ and F4TCNQ. *J. Mater. Chem. C* **8**, 16470–16482 (2020).
25. Campoy-Quiles, M. Will organic thermoelectrics get hot? *Philos. Trans. A Math. Phys. Eng. Sci.* **377**, 20180352 (2019).
26. Scheunemann, D. et al. Rubbing and drawing: generic ways to improve the thermoelectric power factor of organic semiconductors? *Adv. Electron. Mater.* **6**, e2000218 (2020).
27. Derewjanko, D. et al. Delocalization enhances conductivity at high doping concentrations. *Adv. Funct. Mater.* **32**, e 2112262 (2022).
28. Li, M. et al. Controlling the surface organization of conjugated donor-acceptor polymers by their aggregation in solution. *Adv. Mater.* **28**, 9430–9438 (2016).
29. Luzio, A., Criante, L., D'Innocenzo, V. & Caironi, M. Control of charge transport in a semiconducting copolymer by solvent-induced long-range order. *Sci. Rep.* **3**, 3425 (2013).
30. Wang, S. et al. Solvent effects and multiple aggregate states in high-mobility organic field-effect transistors based on pol y(bithiophene-*alt*-thienothiophene). *Appl. Phys. Lett.* **93**, 162103 (2008).
31. Fratini, S., Nikolka, M., Salleo, A., Schweicher, G. & Sirringhaus, H. Charge transport in high-mobility conjugated polymers and molecular semiconductors. *Nat. Mater.* **19**, 491–502 (2020).
32. Shi, X. et al. Relating chain conformation to the density of states and charge transport in conjugated polymers: the role of the β-phase in poly(9,9-dioctylfluorene). *Phys. Rev. X.* **9**, 021038 (2019).
33. Jacobs, I. E. et al. Structural and dynamic disorder, not ionic trapping, controls charge transport in highly doped conducting polymers. *J. Am. Chem. Soc.* **144**, 3005–3019 (2022).
34. Giannini, S. et al. Transiently delocalized states enhance hole mobility in organic molecular semiconductors. *Nat. Mater.* **22**, 1361–1369 (2023).
35. Dash, A. et al. Spontaneous modulation doping in semi-crystalline conjugated polymers leads to high conductivity at low doping concentration. *Adv. Mater.* **36**, e2311303 (2023).
36. Corzo, D. et al. High-performing organic electronics using terpene green solvents from renewable feedstocks. *Nat. Energy* **8**, 62–73 (2022).
37. Chang, J.-F. et al. Enhanced mobility of poly(3-hexylthiophene) transistors by spin-coating from high-boiling-point solvents. *Chem. Mater.* **16**, 4772–4776 (2004).
38. Kim, H. S., Huseynova, G., Noh, Y.-Y. & Hwang, D.-H. Modulation of majority charge carrier from hole to electron by incorporation of cyano groups in diketopyrrolopyrrole-based polymers. *Macromol* **50**, 7550–7558 (2017).
39. Yang, C. Y. et al. Enhancing the n-type conductivity and thermoelectric performance of donor-acceptor copolymers through donor engineering. *Adv. Mater.* **30**, e1802850 (2018).
40. Xiong, M. et al. Efficient n-doping of polymeric semiconductors through controlling the dynamics of solution-state polymer aggregates. *Angew. Chem. Int. Ed.* **60**, 8189–8197 (2021).
41. Yan, X. et al. Approaching disorder-tolerant semiconducting polymers. *Nat. Commun.* **12**, 5723 (2021).
42. Han, J. et al. Blended conjugated host and unconjugated dopant polymers towards n-type all-polymer conductors and high-ZT thermoelectrics. *Angew. Chem. Int. Ed.* **62**, e202219313 (2023).
43. Wolf, C. M. et al. Strategies for the development of conjugated polymer molecular dynamics force fields validated with neutron and X-ray scattering. *ACS Polym. Au* **1**, 134–152 (2021).
44. Cao, Z. et al. Molecular structure and conformational design of donor-acceptor conjugated polymers to enable predictable optoelectronic property. *Adv. Mater.* **35**, e2302178 (2023).

45. Liu, J. et al. N-type organic thermoelectrics of donor-acceptor copolymers: improved power factor by molecular tailoring of the density of states. *Adv. Mater.* **30**, e1804290 (2018).
46. Wang, S. et al. A chemically doped naphthalenediimide-bithiazole polymer for n-type organic thermoelectrics. *Adv. Mater.* **30**, e1801898 (2018).
47. Ma, W. et al. Enhanced molecular packing of a conjugated polymer with high organic thermoelectric power factor. *ACS Appl. Mater. Interfaces* **8**, 24737–24743 (2016).
48. Yang, C. Y. et al. A thermally activated and highly miscible dopant for n-type organic thermoelectrics. *Nat. Commun.* **11**, 3292 (2020).
49. Craighero, M. et al. Impact of oligoether side-chain length on the thermoelectric properties of a polar polythiophene. *ACS Appl. Electron. Mater.* **6**, 2909–2916 (2023).
50. Guo, H. et al. Transition metal-catalysed molecular n-doping of organic semiconductors. *Nature* **599**, 67–73 (2021).
51. Lu, Y. et al. The critical role of dopant cations in electrical conductivity and thermoelectric performance of n-doped polymers. *J. Am. Chem. Soc.* **142**, 15340–15348 (2020).

Methods

Materials

2DPP-2CNTVT and N2200 were purchased from 1-Material. The synthesis of TAM was commissioned to 1-Material. Regioregular P3HT, N-DMBI, TBAF trihydrate and anhydrous CB were purchased from Merck (formerly Sigma-Aldrich). Soda lime square substrates (20 × 20 mm^2) were purchased from Xinyan Technology.

All of the samples were prepared, measured and kept inside a N_2-filled glovebox, unless specified otherwise.

AFM

AFM images were recorded in the semicontact mode using a Next-Solve AFM device by MD-NDT with TESP-SS cantilevers from Bruker (nominal tip radius, 2 nm). Measurements were carried out in air.

AFM-IR

Films were spin coated from 10-mg ml^{-1} solutions in the desired solvent at 100 °C and 1,500 rpm for 60 s, on polished silicon substrates (1 cm^2). Spin-cast films were measured using a nanoIR3 AFM-IR system (Bruker Instruments) coupled to a MIRcat-QT quantum cascade, mid-infrared laser (frequency ranges of 917–1,700 cm^{-1} and 1,900–2,230 cm^{-1} using a range of pulse frequencies between 355 kHz and 1,382 kHz). AFM-IR data were collected in the tapping mode using a Au-coated AFM probe (spring constant, k = 40 N m^{-1}, and resonant frequency, f_0 = 300 kHz) sourced from Bruker. The pulsed mid-infrared laser was tuned to frequencies unique to each component as determined by Fourier transform infrared characterization (DPP at 1,680 cm^{-1}, N-DMBI at 1,552 cm^{-1}, TAM at 1,555 cm^{-1} and TBAF at 1,481 cm^{-1}). The acquired images were flattened using Analysis Studio software and further processed using Gwydion software[52].

GIWAXS

Films were spin coated from 10-mg ml^{-1} solutions in the desired solvent at 100 °C and 1,500 rpm for 60 s, on polished silicon substrates (1 cm^2). Data were acquired using Xenocs Xeuss 3.0 equipped with a Genix 3D Cu source with focused collimation, λ = 1.54 Å and an EIGER2 R 4M detector. The incident angle was set at 0.16° to probe the full thickness of the sample. Collection was carried out in a vacuum. Geometric corrections and data reduction were performed using Xenocs XSACT v.2.8 software.

Electrode deposition

Glass substrates were sequentially sonicated in deionized water, acetone and isopropyl alcohol for 10 min and finally dried with a nitrogen gun. The clean substrates were treated with O_2 plasma for 10 min to remove any organic compounds remaining on the surface. Afterwards, the substrates were transferred to a sputtering chamber for contact deposition. The electrodes for σ and S were sputtered through a shadow mask (10-nm Ti as the adhesion layer plus 50 nm of Au). The electrode array for σ measurement consists of three groups of four bars with a width of 500 µm for either two- or four-point probe measurement with channel dimensions of L = 500 µm and W = 9,000 µm. The electrode array for S measurements consists of two bars with a width of 1 mm and with channel dimensions of L = 6 mm and W = 6 mm.

Transistor fabrication

Here 30-nm-thick Au source and drain contacts were deposited via thermal evaporation through a shadow mask, with dimensions of W = 1,000 µm and L = 30 µm, 40 µm, 50 µm, 80 µm and 100 µm. A 5-mg ml^{-1} solution of the desired polymer was spin coated at 1,500 rpm for 1 min and annealed at 120 °C. CYTOP (CTL-809M) was spin coated as the gate dielectric (4,000 rpm for 30 s and annealed at 90 °C for 20 min). Finally, aluminium bars were patterned as gate contacts through a shadow mask, via thermal evaporation. The fabricated OFETs were transferred to a probe station connected to a Keithley 4200-SCS to measure their I–V characteristics.

Solution doping (co-processing)

2DPP-2CNTVT was dissolved at 10 mg ml^{-1} in the chosen solvent and left under stirring at 80 °C for at least 2 h before blending. Dopants were dissolved in CB at 20 mg ml^{-1} and left stirring at room temperature for at least 8 h before blending. Once prepared, the dopant solution can be stored and used in a N_2 atmosphere for up to 1 year, without any observed degradation in its electronic properties. Solution doping was performed by mixing aliquots of 2DPP-2CNTVT and the dopant stock solution at the desired ratio. The host–dopant solutions were left under stirring at 100 °C for 10 min before deposition. Solutions of doped CPs were deposited on top of the Au electrodes via spin coating at 1,000 rpm for 30 s and transferred to a hotplate for annealing at 120 °C for 30 min, yielding films with an average thickness of 20 nm as measured by AFM.

Sequential doping

2DPP-2CNTVT films were cast following the previous methodology but omitting the addition of dopant aliquots. Instead, N-DMBI and TAM stock solutions in methanol were prepared and sequentially diluted to achieve the desired concentration. The CP films were soaked in the dopant solution with the desired concentration for 10 min. The films were then flushed with a N_2 stream to dryness, and annealed for 30 min in a hotplate at 100 °C.

Electronic characterization

The fabricated films were transferred to a probe station connected to a Keithley 4200-SCS device. I–V curves were recorded using two-point probe electrode arrays; the channel resistance was calculated from the slope of the I–V curve and σ was calculated considering the geometric factors of the channel. Temperature-dependent σ was obtained using a thermal chuck; the temperature was recorded using a T-type thermocouple connected adjacent to the channel for I–V measurement. The activation energies were calculated using the Arrhenius equation. S was measured using the voltage measure unit (VMU) of the Keithley 4200-SCS. The thermal gradient was generated using a Peltier device placed directly on top of the film, using thermal grease to promote homogeneous heat transfer. A heat sink was placed on the cold side to maintain a homogeneous temperature gradient across the whole sample throughout the measurement. The thermovoltage of the channel was recorded along with a constantan wire as a reference. The S value was calculated from the slope of the thermovoltage of the sample versus that of the constantan wire.

Temperature-dependent TE properties

We dissolved 2DPP-2CNTVT in CB at 20 mg ml^{-1} and blended it with 20-mg ml^{-1} N-DMBI in CB at the optimized ratio (20 mol%). The film was spin coated at 400 rpm for 2 min on a masked chip from Linseis, obtaining a 2-µm-thick film. The chip contains van der Pauw and 3ω electrode arrays for the simultaneous measurement of σ, S and κ in the in-plane orientation. The sample was transferred to the vacuum chamber of a Linseis thin-film analyser for automated temperature-dependent measurements.

Photoelectron spectroscopy

Thin-film polymer samples were prepared by spin coating a polymer solution in CB (2 mg ml^{-1}) on a clean silicon substrate coated with a 10-nm Ti adhesion layer and 100 nm of Au. The films were transferred from N_2 to a vacuum using an airtight transferring arm, preventing sample exposure to air.

Ultraviolet photoelectron spectroscopy measurements on thin polymer films were performed in an ultrahigh-vacuum chamber (base pressure, 10^{-10} mbar) equipped with a Sphera II EAC 125 7-channeltron electron analyser calibrated with the Fermi edge of clean polycrystalline silver. The spectra were recorded at a pass energy of 10 eV using the He I line (21.22 eV). The work function of the samples was determined from

the secondary electron cut-off of the ultraviolet photoelectron spectra, as described elsewhere, with an uncertainty of ±0.05 eV (ref. 53).

Low-energy inverse photoemission spectroscopy measurements were performed in the isochromatic mode (base pressure, 10^{-9} mbar) using a custom-built setup with a solid-state photomultiplier tube detector (Hamamatsu R585) mounted outside of the vacuum region and equipped with a bandpass filter of 280 nm (Semrock) with a narrow wavelength window of 10 nm. The system is based on a previously reported setup[54]. Low-energy inverse photoemission spectroscopy measurements were performed on the same samples after the ultraviolet photoelectron spectroscopy measurements, in an interconnected ultrahigh-vacuum chamber without breaking the vacuum. The onset energies of the frontier molecular orbitals were estimated by deconvoluting the spectra using Gaussian functions and a Tougaard background.

Ultraviolet–visible–near-infrared spectroscopy

The absorption spectra were recorded using a Filmetrics F-20 series system. The spectra were recorded from the same films as those used for σ and S measurements without exposure to air.

Data availability

The main data supporting the findings of this study are available within the Article and its Supplementary Information. Alternative formats for raw data files may be requested from the corresponding authors. 2D GIWAXS diffractograms of P3HT, N2200 and 2DPP-2CNTVT are available via the KAUST repository at https://doi.org/10.25781/KAUST-1709U (ref. 55). Source data are provided with this paper.

Code availability

Code for the KMC and three-phase model is available from M.K. upon request.

References

52. Nečas, D. & Klapetek, P. Gwyddion: an open-source software for SPM data analysis. *Cent. Eur. J. Phys.* **10**, 181–188 (2012).
53. Sharma, A. et al. Insights into the oxidant/polymer interfacial growth of vapor phase polymerized PEDOT thin films. *Adv. Mater. Interfaces* **5**, 1800594 (2018).
54. Yoshida, H. Near-ultraviolet inverse photoemission spectroscopy using ultra-low energy electrons. *Chem. Phys. Lett.* **539–540**, 180–185 (2012).
55. Rosas Villalva, D. & Baran, D. GIWAXS of conjugated polymers, 2DPP-2CNTVT, P3HT, and N2000. *KAUST Research Repository* https://doi.org/10.25781/KAUST-1709U (2024).

Acknowledgements

D.R.V. and D.B. thank the King Abdullah University of Science and Technology (KAUST) Office of Research Administration (ORA), award no. ORA-CRG2022-4668. We also would like to thank C. Muller for fruitful discussions on the influence of ionized species on the assembly of the morphology of doped CPs. M.K. thanks the Carl Zeiss Foundation for financial support. D.B., G.C. and S.M. acknowledge support from the UK–Saudi Challenge Fund grant from the British Council's Going Global Partnerships programme.

Author contributions

D.R.V. and D.B. supervised the work. D.R.V. conceived the idea and wrote the manuscript, as well as performed the AFM and GIWAXS characterizations. D.D. and M.K. performed and supervised the computational modelling. D.R.V., Y.L. and Y.Z. fabricated the devices and measured the electronic properties. D.R.V., Y.Z. and S.J. determined the HSPs. A.B. and X.G. carried out the AFM-IR characterization and analysis. A.S. performed the ultraviolet photoelectron spectroscopy and low-energy inverse photoemission spectroscopy measurements. J.H. performed the density functional theory calculations. O.Z.A. and Y.Z. performed the thermal conductivity measurements and analysis. M.G.-R. provided technical assistance with setup designs for characterization. S.M. and G.C. performed the STM measurements. All authors contributed to manuscript editing and revision.

Competing interests

The authors declare no competing interests.

Additional information

Extended data is available for this paper at https://doi.org/10.1038/s41563-025-02207-9.

Supplementary information The online version contains supplementary material available at https://doi.org/10.1038/s41563-025-02207-9.

Correspondence and requests for materials should be addressed to Diego Rosas Villalva, Martijn Kemerink or Derya Baran.

Peer review information *Nature Materials* thanks the anonymous reviewers for their contribution to the peer review of this work.

https://doi.org/10.1038/s41563-025-02207-9

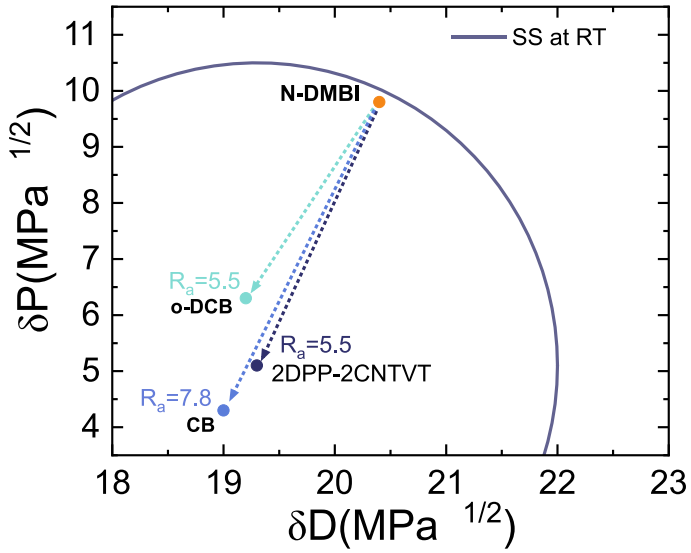

Extended Data Fig. 1 | N-DMBI's R_a vs solvents and polymer. The R_a between N-DMBI and 2DPP-2CNTVT is equal to that of N-DMBI and o-DCB this means that N-DMBI is equally likely to interact with either of them. N-DMBI's R_a to CB is larger than that of 2DPP-2CNTVT meaning that the dopant will more likely interact with the CP.

https://doi.org/10.1038/s41563-025-02207-9

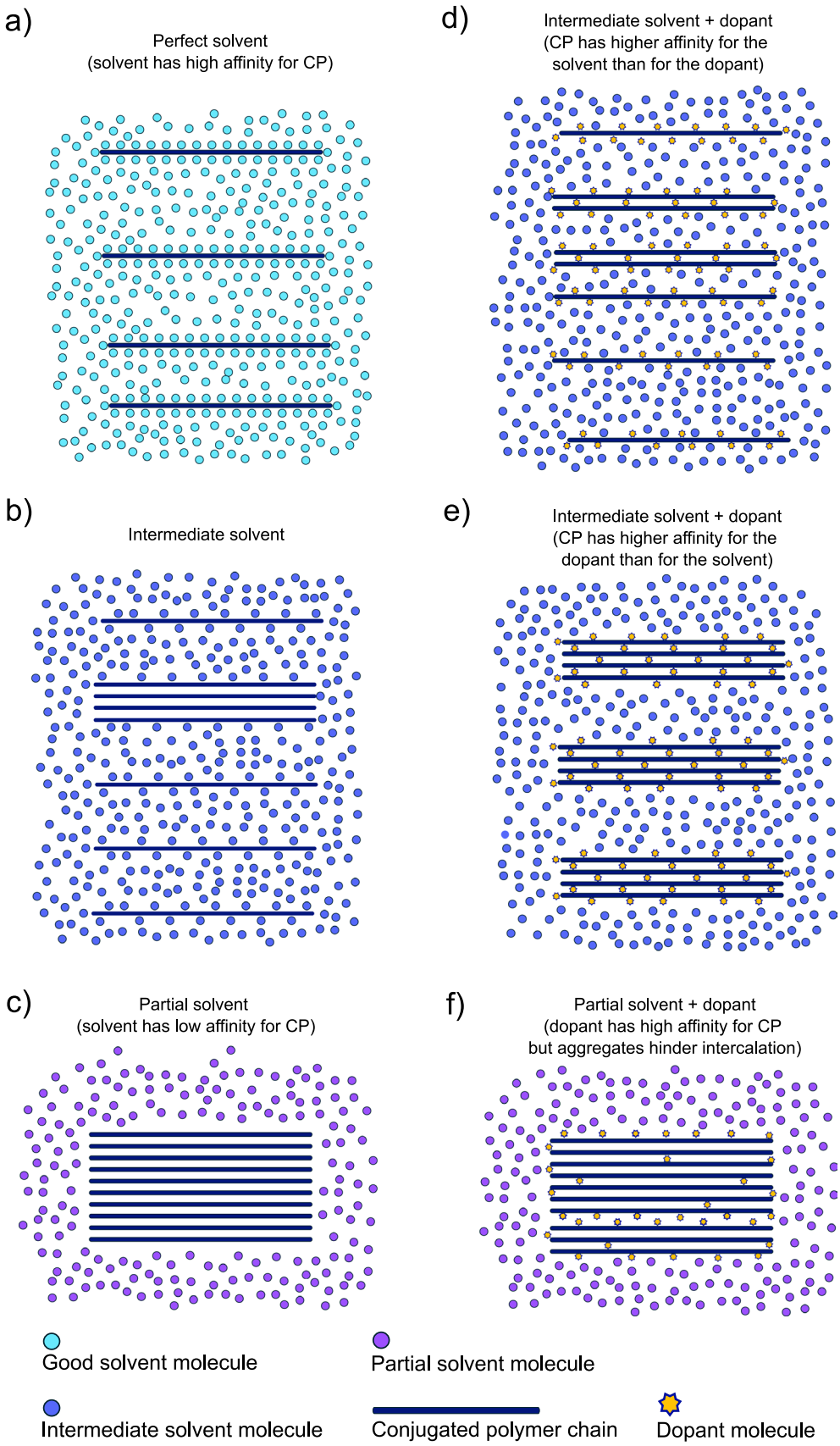

Extended Data Fig. 2 | See next page for caption.

https://doi.org/10.1038/s41563-025-02207-9

Extended Data Fig. 2 | CP solution aggregation behaviour upon addition of dopant. a) In a perfect solvent, polymer chains are fully dissociated. **b**) In an intermediate solvent, polymer chains are both fully dissociated and forming small lamellar aggregates. **c**) Partial solvents give result to large polymer aggregates. Addition of dopant in a perfect solvent result in good CP-dopant intercalation owing to full dissociation of polymer aggregates, without a significant change in the aggregation behaviour. This is similar to adding a dopant in an intermediate solvent, where the CP has lower or affinity for the dopant than for the solvent (**d**). This should produce minimal effect on the resulting thin film morphology. In contrast, adding a dopant to an intermediate solvent (**e**) where the CP has similar or higher affinity for the dopant than for the solvent, a competing interaction is triggered that increases the polymer aggregates in solution. This case should result in an increase in the crystalline fraction and the EFR. Finally, in (**f**), adding dopants in a bad solvent should result in a decrease in the aggregates, due to the dopant attempting to intercalate with the CP. This should produce a film with hindered crystallinity and lower EFR.